

Discovery of Spatter Constitutive Models in Additive Manufacturing Using Machine Learning

Olabode T. Ajenifujah^a, Amir Barati Farimani^{a,b,c},

^a*Department of Mechanical Engineering, Carnegie Mellon University, Pittsburgh, 15213, PA, USA*

^b*Department of Chemical Engineering, Carnegie Mellon University, Pittsburgh, 15213, PA, USA*

^c*Machine Learning Department, Carnegie Mellon University, Pittsburgh, 15213, PA, USA*

Abstract

Additive manufacturing (AM) is a rapidly evolving technology that has attracted applications across a wide range of fields due to its ability to fabricate complex geometries. However, one of the key challenges in AM is achieving consistent print quality. This inconsistency is often attributed to uncontrolled melt pool dynamics, partly caused by spatter which can lead to defects. Therefore, capturing and controlling the evolution of the melt pool is crucial for enhancing process stability and part quality. In this study, we developed a framework to support decision-making towards efficient AM process operations, capable of facilitating quality control and minimizing defects via machine learning (ML) and polynomial symbolic regression models. We implemented experimentally validated computational tools, specifically for laser powder bed fusion (LPBF) processes as a cost-effective approach to collect large datasets. For a dataset consisting of 281 varying process conditions, parameters such as melt pool dimensions (length, width, depth), melt pool geometry (area, volume), and volume indicated as spatter were extracted. Using machine learning (ML) and polynomial symbolic regression models, a high R^2 of over 95 % was achieved in predicting the melt pool dimensions and geometry features on both the training and testing datasets, with either process conditions (power and velocity) or melt pool dimensions as the model inputs. In the case of volume indicated as spatter, the value of the R^2 improved after logarithmic transforming the model inputs, which were either the process conditions or the melt pool

dimensions. Among the investigated ML models, the ExtraTree model achieved the highest R^2 values of 96.7 % and 87.5 %. With respect to the symbolic regression model, R^2 values of 85 % and 82 % were achieved on the training and testing datasets, respectively. Our study culminated in the discovery of symbolic equations based on model inputs in the polynomial fitting model for all investigated parameters, thereby providing interpretable evaluations of the feature importance.

Keywords: Additive Manufacturing, Symbolic Regression, Process Map, Machine Learning, Defects.

1. Introduction

Laser Powder Bed Fusion (LPBF) is a popular metal additive manufacturing (AM) process that has demonstrated high precision and remarkable performance in producing complex part geometries and internal structures with micron-scale precision. The operating process of Laser Powder Bed Fusion (LPBF) involves guiding a laser using a scanning galvanometer to selectively melt a layer of powder deposited on a build plate. Once solidification occurs, the next layer of powder is spread and the process is repeated iteratively until the final part is complete [1]. In addition, LPBF offers significant advantages, including design flexibility, an automated method for building parts directly at their point of use from CAD files, and reduced material waste. These benefits have facilitated its adoption in various industries, including aerospace, automotive, medicine, energy, and prototyping [2, 3]. However, despite its increasing application in different sectors, compared to other forms of manufacturing processes such as rolling, casting, and machining, LPBF still occupies a low market share, which is attributed to its low rate of part production and poor quality control. A popular approach to remediate low part production involves using multi-lasers, which, however, increases the defect formation rate. The efficacy of state-of-the-art methods for quality control is assessed by comparing the properties and performance of the finished part with the target

standard, although variability and suboptimal performance are still observed.

Identifying optimal process conditions typically relies on costly and time-intensive trial-and-error experiments across a wide range of process parameters. This challenge has motivated the use of 3D numerical modeling tools, which can effectively capture the complex phenomena occurring during melting and provide insights into parameters that are difficult or impossible to measure using current *in situ* experimental techniques. However, a high-fidelity AM simulation package that will account for all of the complex physics in AM is computationally expensive. As a result, increasing attention is being directed towards a robust smart AM manufacturing tool, which has been dubbed a solution to match the desired properties and performance of parts and AM tools [4]. This approach involves developing a digital twin of the LPBF process, which will be capable of mirroring the real-time evolution of part-building processes, displaying key measurements, and forecasting future events during laser-material interactions. This type of system will enhance the detection of faults or anomalies during the printing process through the integration of a sensitive control system to mitigate or prevent the intricacies that may occur during the printing process. The core component of the digital twin will be the integration of experimental datasets, system modeling analysis, and ML models. ML enables predictive and performance insights that can be difficult to uncover through traditional physics-based modeling approaches due to the high computation cost. [5–9]. Monitoring the formation and dynamic processes that occur in the melt pool is one of the crucial aspects of LBPF operation that can improve quality control by providing an understanding of the underlying processes that take place in relation not only to the process conditions, but also to the material types that govern the nature of the melt pool, the microstructure, and the mechanical properties [2]. Consequently, defect formation, such as porosity, surface roughness, residual stresses, warping, cracking, and delamination that can influence quality control, will be further elucidated and prevented.

The general characteristics of the melt pool that have been popularly monitored to

understand the formation of defects or the properties of built parts are dimensions [10–14], shape[15–19], temperature distribution [20–26], oxygen content [27–31], and pressure [29]. Many studies have been reported on coupling ML with monitoring parameters collected either through experimental or modeling methods to accelerate the interpretation of system behavior. Xiao et al. [4] predicted the future melt pool area using the history of the previous construction. They first filtered out noise using a convolutional neural network (CNN)-based model, then quantitatively estimated future melt pool areas using an artificial neural network (ANN) trained on scanning history, particularly past melt pools. This approach significantly reduced the average relative error magnitude (AREM) to 2.8% compared to 14.8% with the existing Neighboring Effect Modeling Method (NBEM). Akbari et al. [32] predicted the dimensions of the melting pool using ML models, where the process parameters and the material properties are curated from different source of published literatures. Zhang et al. [33] implemented LSTM-based approach to estimate the area of the melt pool with accuracy of 90.7 %, then used Melt Pool Generative Adversarial Network to synthesize the images of the melt pool and achieve a structural similarity score of 0.91. Wang et al. [34] implemented a machine learning-assisted approach based on a deep neural network to demodulate the optical signal to thermal distribution and significantly improve spatial resolution to 28.8 $\mu\text{m}/\text{pixel}$ spatial resolution and 10 kHz sampling frequency, ideal for measuring the sharp thermal gradient and cooling rates in the L-PBF process. Scime et al. [35] used a high-speed camera to capture the images of the molten pool, then proposed an unsupervised learning algorithm to distinguish the molten pool and identify defects.

Extending quality control to the monitoring of the ejection of the spatter from the melt pool can provide information on the state or stability of the melt pool as defects develop [36–39]. In-homogeneity fusion and thermal gradient caused by spatter can be a source of crack initiation sites [40]. The traveling spatter can absorb the laser radiation or reflect it, causing a fluctuation in the intensity of the laser [41]. Limited research has explored

the integration of machine learning (ML) models with spatter formation. Most studies in this area have focused mainly on spatter detection by coupling ML with computer vision or by classifying spatter according to process conditions or signals [3, 42–46]. However, these approaches do not explain the underlying mechanisms that govern the ejection rate of the spatter, which fluctuates according to the process conditions and the state of the melt pool. Previously, we implemented machine learning (ML) to classify and detect slight variations in the measured parameters between the spatter and the melt pool at 5 μ s. This approach revealed the ranking of different measured parameters based on their importance in spatter ejection. To enhance interpretability, we applied an explainable AI technique known as SHapley Additive exPlanations (SHAP), which allowed us to identify the range of the feature values that positively contribute to spatter predictions [5].

Building upon our previous investigations, this work employs both ML regression and symbolic regression to predict melt pool features measured at a stable state. These features include dimensions (length, width, and depth), geometric properties (cross-sectional area and volume), and the volume indicated by spatter. We collect the data set of the spatter count versus process conditions by augmenting OpenFOAM and FLOW-3D simulations via ML model developed for binary classification task for spatter/melt pool predictions. The motivation behind the techniques lies on the trade-off between the capability and computational costs of both simulation tools. FLOW-3D incorporates certain restrictive assumptions to reduce computational costs, which limit its ability to simulate spatter accurately. Specifically, it approximates the keyhole gas dynamics using estimates of recoil pressure and mass transfer, rather than directly simulating them. Furthermore, FLOW-3D does not account for the tangential surface tension component [47, 48]. In contrast, our OpenFOAM model directly simulates keyhole gas dynamics and incorporates tangential surface tension. The analysis indicated that the melt pool features can be predicted with a high R^2 value from the process conditions (power and velocity). Similarly, the volume indicated as spatter can

be predicted with a high R^2 value from either the process conditions or the dimensions of the melt pool, as shown in Fig. 1. Our findings not only demonstrate the interconnection between process conditions, melt pool features, and spatter counts, but also provide an interpretable mathematical expression of the parameters derived from the input variables through symbolic regression models, which could be crucial for process optimization.

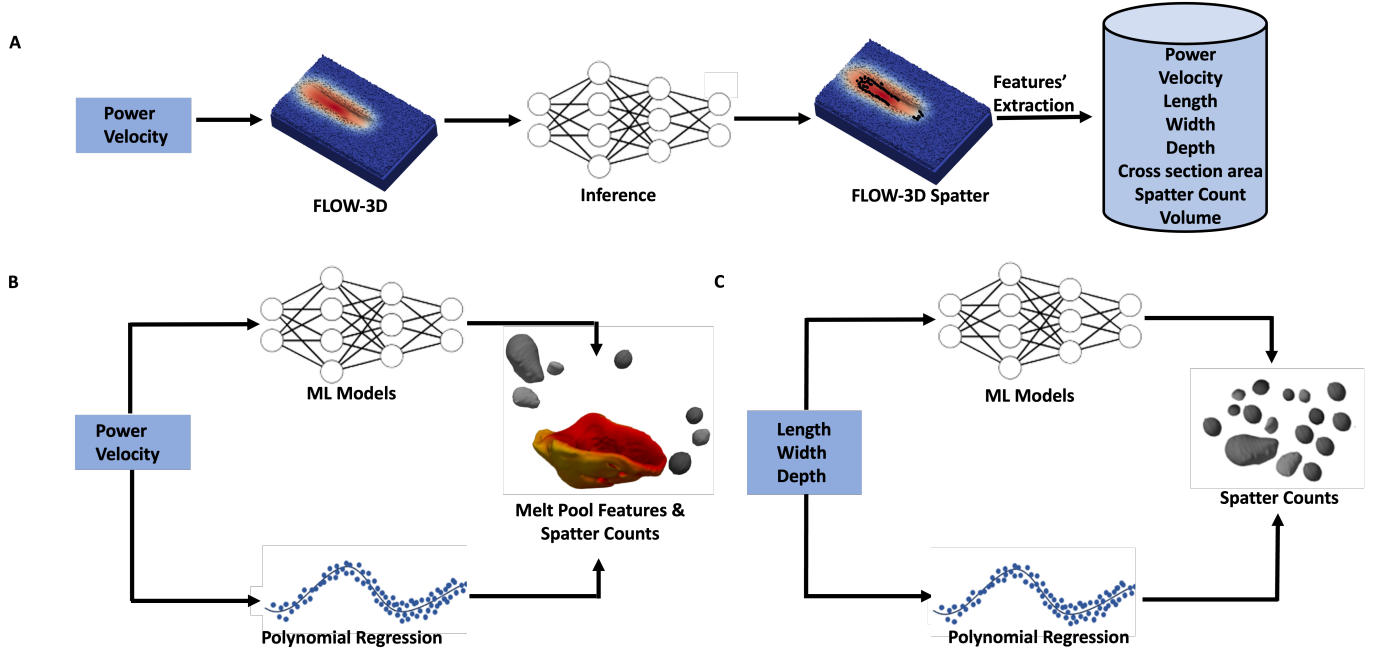


Figure 1: Spatter dataset generated using OpenFOAM, a computationally expensive tool, was trained for classification task to differentiate between the two classes. Using the model as an inference, spatter count was predicted on a FLOW-3D, which is 18 times less computationally expensive tool. (a) Datasets consisting of process conditions, melt pool dimensions, geometry, and spatter count were collected from 281 FLOW-3D experiments (b) The process conditions was used as an input to either the ML model or polynomial regression to predict the melt pool dimensions, geometry features and the spatter count (c) The melt pool dimension was used as an input to either the ML model or polynomial regression to predict the spatter count

2. Methods

2.1. LPBF Simulation Tools

A CFD model was developed to analyze LPBF simulation using OpenFOAMv2012 using the `icoReactingMultiphaseInterFoam` (IRMIF) solver [2, 49, 50]. The IRMIF solver is based

on the volume-of-fluid (VOF) method, where each phase is immiscible, and a clear boundary between each phase is calculated. The IRMIF solver handles fluid mechanics, including turbulent flow, laser beam sources with arbitrary beam shapes, heat transfer, and phase transitions such as solidification, melting, and evaporation. However, the solver did not account for the Marangoni effect due to the absence of the tangential component of the surface tension. The continuity and transient Stokes equation as described in equation (3) and (4) respectively.

$$\frac{\partial \rho}{\partial t} + \nabla \cdot (\bar{\rho} \vec{U}) = 0 \quad (1)$$

$$\frac{\partial(\rho \underline{u})}{\partial t} + \nabla(\rho \underline{u} \otimes \underline{u}) = \nabla \left\{ -p \cdot \underline{I} + \mu [\nabla \underline{u} + (\nabla \underline{u})^T] \right\} + \underline{F} \quad (2)$$

where ρ is the density, \underline{u} is the fluid flow velocity vector, t is the time, p is the pressure, \underline{I} is the identity tensor, μ is the dynamic viscosity, and \underline{F} is the volume force vector. The energy equation in equation (5) was used to compute the temperature field.

$$\rho \frac{\delta E}{\delta t} = -\rho \vec{\nabla} \cdot \vec{u} E + \vec{\nabla} \cdot (\lambda \vec{\nabla} T + \vec{\tau} \cdot \vec{u}) \pm S_h \quad (3)$$

where E is the mixed energy, λ is the thermal conductivity. Further detail about the simulation can be found in our previous work [5].

FLOW-3D (v11.2) simulations are performed to accelerate process map development. FLOW-3D is a multiphysics simulation software produced by Flow Science, which provides more rapid estimations of the melt pool behavior than OpenFOAM. To create a dataset of FLOW-3D simulations, 281 SS316L single-track bare plate experiments are performed at varying processing parameters for a total length of 600 μs . During simulation, the FLOW-3D package solves the equations that describe mass transfer, momentum transfer, and energy transfer during the melting process. This simulation is carried out on a structured Cartesian mesh, with mesh elements sized at 10 μm . More specific information on the equations solved and the physical phenomena considered during the simulation can be found in [21, 25, 48,

51, 52].

2.2. Spatter Process Map Generation

This study uses a range of computational techniques and machine learning methods to analyze OpenFOAM 3D simulation data and FLOW-3D to establish a spatter process map. Features such as position (x , y , z), velocity components (v_x , v_y , v_z), velocity magnitude, pressure, temperature, and density were extracted from the spatter and the melt pool following the methodology we previously outlined [5]. These features of the melt pool and the spatter were passed into the ML model for the classification task. The prediction of spatter on the FLOW-3D dataset necessitates the extraction of similar features from the FLOW-3D as the OpenFOAM. The results of 281 different process conditions from the FLOW-3D dataset were pre-processed to extract the liquid fraction from the simulation as the melt pool. The velocity magnitude is calculated from the three velocity components (v_x , v_y , v_z) using Equation (4), producing scalar values that represent the speed at each point in the 3D grid.

$$U_{\text{magnitude}} = \sqrt{v_x^2 + v_y^2 + v_z^2} \quad (4)$$

The features of the OpenFOAM dataset (velocity components (v_x , v_y , v_z), velocity magnitude, pressure, temperature, and density) are entered into the ML model for training and testing purposes. Before using the trained ML model as an inference for FLOW-3D datasets, the FLOW-3D dataset is pre-processed by aligning the range of each feature with OpenFOAM dataset. The FLOW-3D data set that represents one process condition is a representative of the average of the feature from the point the melt pool is determined to be stable to the end of the simulations.

2.3. Ensemble Learning and Polynomial Regression

This study performs a regression task using the ML and polynomial regression models for the prediction of the features of the melting pool or the spatter as presented in Figure 1. The

following ML models are screened with the datasets: Extremely Randomized Trees (Extra-Trees), Extreme Gradient Boosting (XGB), Random Forest (RF), Bagging, and k-Nearest Neighbors (KNN). The descriptions of the ML model are in Appendix A.1.1. To predict the spatter count, two groups of features are identified, which are the process parameters and the dimensions of the melt pool. To predict the dimension and geometry of the melt pool, only the process parameters were implemented as input features of the model. These features are inputted into either the ML or polynomial regression models. Polynomial regression is particularly effective when linear models are insufficient to capture the complexity of the data. In this case, the degree of the polynomial was vary in the range 2-6, allowing for higher-order interactions among the independent variables. A pipeline was constructed that combined polynomial feature transformation and linear regression. This pipeline streamlined the process of applying polynomial transformation and fitting the regression model. The Linear Regression model was trained on the transformed features, establishing the relationship between the independent and dependent features. Following model training, the coefficients and intercepts of the regression model were extracted. These values were used to formulate the polynomial equation, which expresses the relationship between the input variables and the target variable. The equation provides an explicit representation of the learned model, highlighting the contribution of each feature interaction to the prediction of the desired variable. The predictive performance of the model was evaluated using the coefficient of determination (R^2). The R^2 score reflects the proportion of variance in the dependent variable explained by the independent variables, with higher values indicating a better fit.

3. Results and Discussion

3.1. Properties variations and correlations across process conditions

The melt pool dynamics in the LPBF process is shaped by a complex interplay of forces: gravity, Marangoni forces, buoyancy, and recoil pressure. Gravity exerts a uniform downward pull, influencing the overall shape and stability of the molten region. In contrast, Marangoni forces arise from surface tension gradients caused by temperature and compositional variations, driving fluid flow from hotter, lower-surface-tension regions to cooler, higher-surface-tension areas. These forces create convective currents that redistribute heat within the melt pool. Buoyancy, driven by density differences in the molten material due to temperature gradients, induces additional convective flows, with hotter, less dense material rising and cooler, denser material sinking. Together, gravity, Marangoni forces, and buoyancy determine the internal flow patterns and stability of the melt pool.

The recoil pressure, generated by rapid vaporization at the surface of the melt pool, introduces localized pressure gradients that push the molten material away from the high-energy impact zone. This force influences the depth and shape of the melt pool and plays a significant role in material expulsion and spatter formation. The effect of these forces varies across four primary process regions: high-power low-speed, high-power high-speed, low-power low-speed, and low-power high-speed. In the low-speed, high-power region, recoil pressure and Marangoni forces often dominate, deforming the melt pool and potentially creating keyholes. Significant energy is concentrated in a small area for an extended period of time, producing a deep and wide melt pool with high volume and intense spatter, as shown in Figure 2 (b, c, d, e, f) due to strong recoil pressure and Marangoni-driven recirculation. In the high-power, high-speed region, the laser moves quickly over the material, resulting in a long, narrow melt pool with moderate depth, area, and volume, as shown in Figure 2. Although the recoil pressure is high, the limited interaction time keeps the melt pool from becoming excessively deep or wide, and the generation of spatter is moderate.

In the low-power low-speed region, the melt pool is shallow and broad with minimal spatter because a lower energy input produces less recoil pressure and vaporization. This configuration favors precision and surface quality over depth, making it suitable for applications where fine control is prioritized. Lastly, in the low-power high-speed region, the melt pool is very shallow and narrow, with negligible spatter because low-power and high-speed minimize melting. Gravity and buoyancy have a more pronounced effect in this region. Each of these regions produces distinct melt pool geometries, enabling manufacturers to tailor process parameters for specific design requirements, whether for high depth and volume or minimal surface impact.

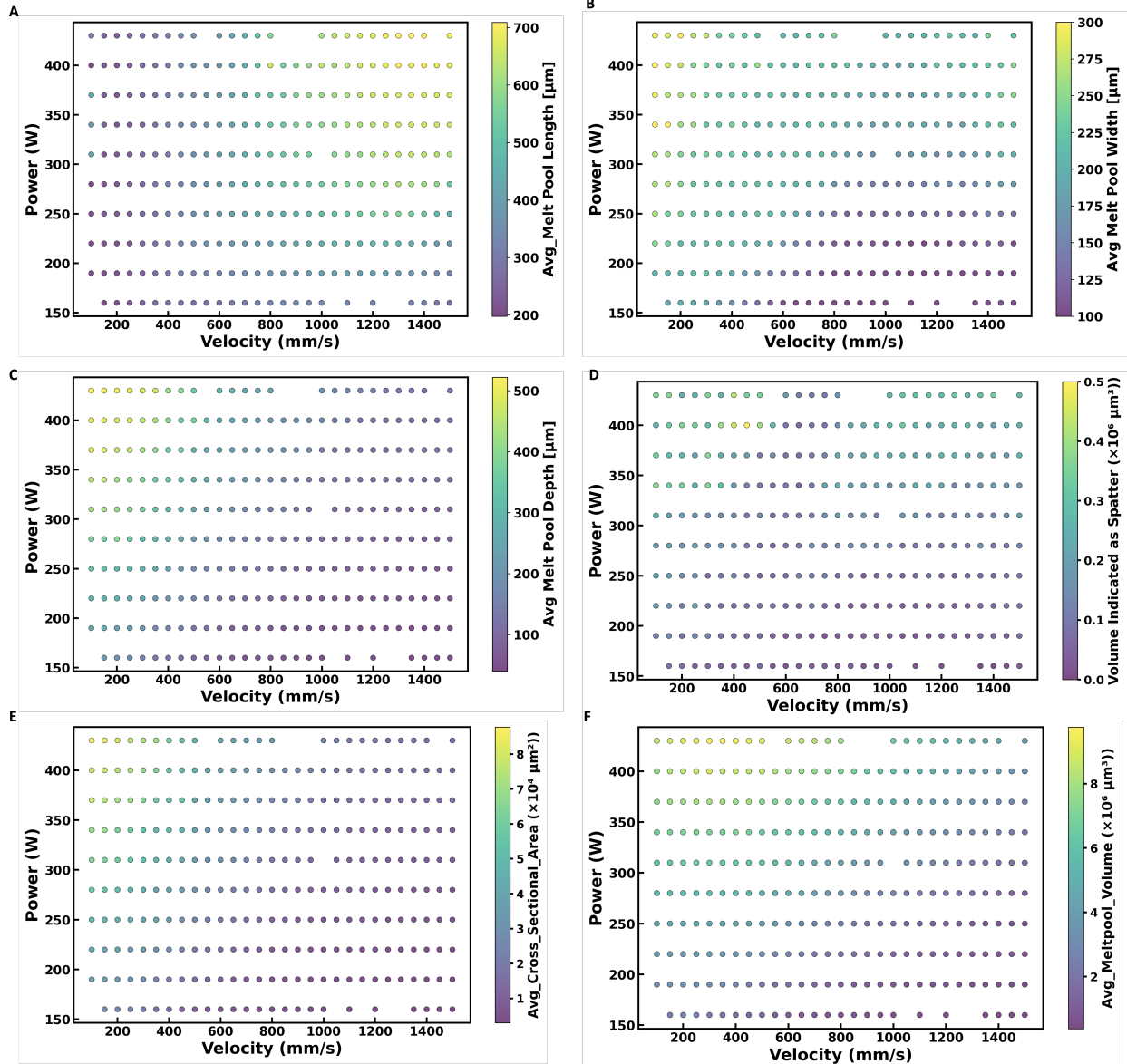


Figure 2: Distribution of the extracted parameters from the simulation of LPBF (a) Melt pool length (b) Melt pool width (c) Melt pool depth (d) Volume indicated as spatter (e) Melt pool cross section area (f) Melt pool volume

Figure 3 shows the correlation matrix that shows the Pearson correlation coefficients between pairs of variables, indicating the strength and direction of their linear relationships. The diagonal values are all 1.0, since each variable is perfectly correlated with itself. The color scale ranges from -1 (blue, indicating a strong negative correlation) to +1 (red, indicating a strong positive correlation). Positive correlations are shaded in red hues, while negative correlations appear in blue hues. Notable relationships include strong positive correlations between the width, depth, cross-sectional area, and volume of the melt pool, with coefficients close to or above 0.8, indicating that as one of these variables increases, the corresponding pairing variable increases as well. Furthermore, the power and volume indicated as spatter show a high correlation (0.79), suggesting that higher power levels may lead to higher volumes of spatter. Moderate positive correlations are observed between power and width (0.68), power and depth (0.50), and power and avg melt pool volume (0.79), which implies that an increase in power generally corresponds to increases in these variables. In contrast, velocity exhibits negative correlations with depth (-0.78), cross-sectional area of avg (-0.77) and volume of the avg melt pool (-0.57), indicating that higher velocities are associated with smaller depths, cross-sectional areas, and volumes of the melt pool. Weak correlations were observed in the following combination of variables: Length and width (-0.13), length and avalanche meltpool volume (-0.18), velocity and volume indicated as splinter (-0.19), and length and volume indicated as splinter (0.15). These low correlation values imply that these pairs of variables have minimal linear relationships, which means that changes in one variable do not consistently predict changes in the other.

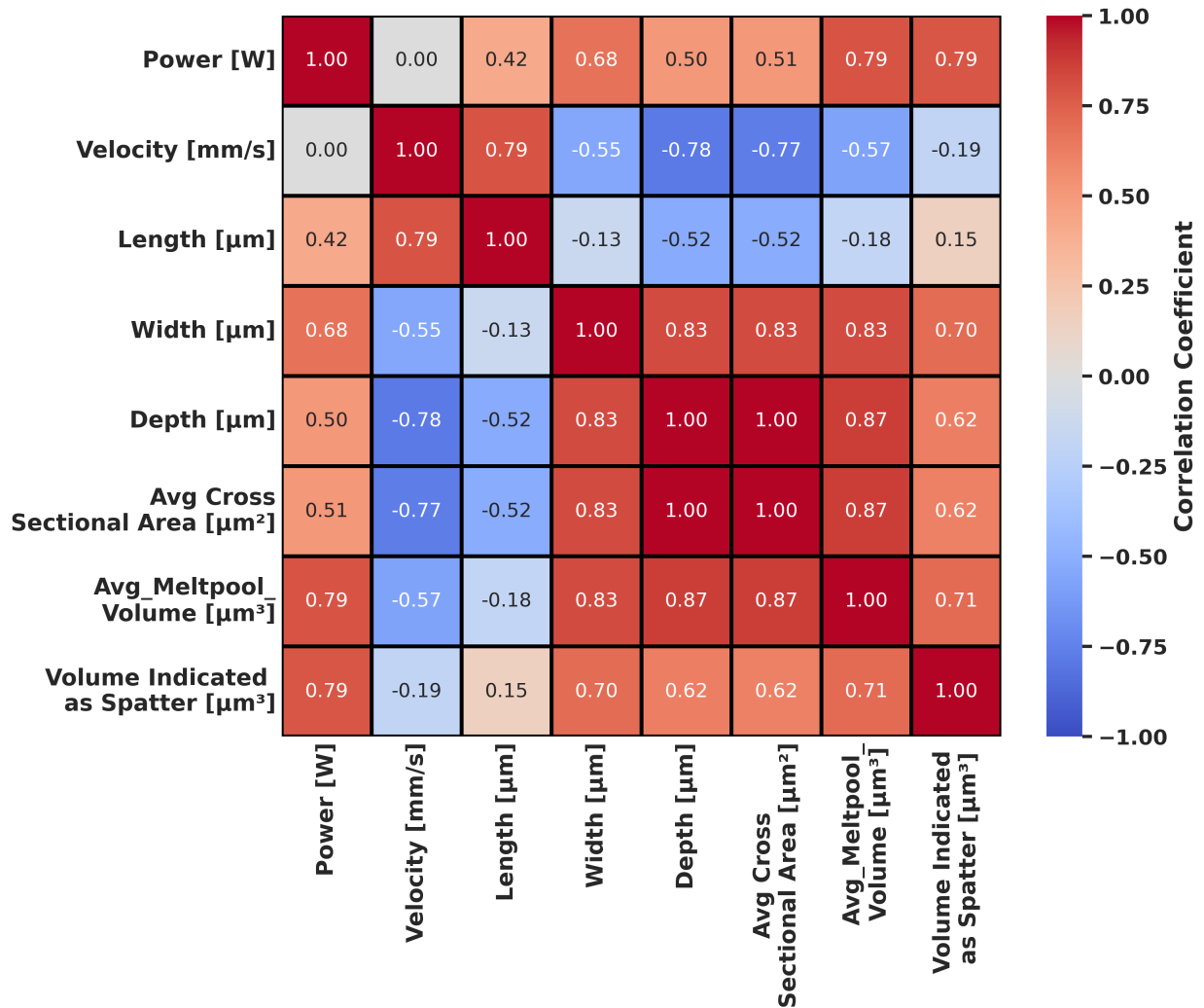


Figure 3: A correlation matrix displays the Pearson correlation coefficients between pairs of variables in the process conditions, melt pool dimensions and geometry

3.2. Machine Learning regression prediction

The performance of five machine learning algorithms: Random forests (RF), extra trees (ExtraTree), bagging, k-nearest neighbors (KNN), and gradient boost (GB) were evaluated using input features derived from process conditions and melt pool dimensions. With process conditions (power and velocity) as input, the models can predict the dimensions of the melt pool (length, width, and depth), geometric features (area and volume) and the volume indicated as spatter as shown in Figure 1b. Furthermore, using the dimensions of the melting pool (length, width, and depth) as input, the models can predict the volume indicated as a spatter, as shown in Figure 1c. The hyperparameters implemented for the ML models, such as the number of estimators, the maximum depth, the number of neighbors, and the learning rates, are listed in Table 1. Table 2 summarizes the performance metrics used, including R^2 scores for both training and testing sets, as well as mean absolute error (MAE) for both sets. The R^2 score measures the proportion of variance in the dependent variable that is predictable from the independent variables, while the MAE quantifies the average magnitude of the prediction errors, regardless of their direction. Using power and velocity as the model input, the R^2 predictions for the melt pool length data set show strong performance, with the training data set R^2 values exceeding 98%, and the lowest R^2 for the test dataset reaching 95.6% when using the ExtraTree model. Similarly, high R^2 values were observed for depth, melt pool area, and volume, with R^2 scores for training and test sets exceeding 97%. For depth, R^2 values remained consistently high ($> 97\%$) on both the training and the test data. However, a slight drop in the R^2 prediction was observed for width, with the lowest values appearing in the KNN model, where the training and test R^2 scores were 97.4% and 91%, respectively. A further drop in the prediction of the volume indicated as spatter; in this case, the most promising model was RF, with training and test R^2 values of 94.1% and 83.4%, respectively.

Introducing logarithmic terms to the input was considered a strategy to improve accuracy,

as it can better capture nonlinear relationships between the variables. Upon adjusting the input of the model from power and velocity to power, velocity and $\log(\text{Velocity})$, the ExtraTree model demonstrated the most significant improvement in test accuracy. The test accuracy of ExtraTree increased from 79.6% to 84.1%, while its training accuracy improved from 91.4% to 94.3%. This enhancement highlights the potential of input manipulation through logarithmic transformations to improve prediction accuracy by effectively modeling nonlinear dependencies.

Because power and velocity are fixed during a particular process operation, our results demonstrate that these process conditions can effectively predict the characteristics of a stable melt pool. When using the dimensions of the melt pool (length, width and depth) as inputs into the ML models to predict the volume indicated as a spatter, we observed an accuracy comparable to when power and velocity were used as inputs. The KNN model achieved the highest test accuracy at 82.3%, with a training accuracy of 85.8%. Although the Extra Tree model had the highest training accuracy at 90.5%, its test accuracy was slightly lower at 80.1%. Upon introducing logarithmic terms to the model input, changing them from length, width, and depth to $\log(\text{length})$, $\log(\text{width})$, $\log(\text{depth})$, $\log(\text{width})$, and $\log(\text{depth})$, the most significant improvement was observed in the Extra Tree model, with training and test accuracies reaching 95.8% and 87.5%, respectively. This improvement highlights the effectiveness of incorporating logarithmic terms to capture the nonlinear relationships within melt-pool dimensions, enhancing the prediction of volume indicated as spatter.

Table 1: The hyperparameters used to train different ML models with varying inputs and outputs.

Model	Input	Output	n.estimators	max_depth	n.neighbors	LR
RF	[Power, Velocity]	[Length]	5	8		
ExtraTree	[Power, Velocity]	[Length]	5	7		
Bagging	[Power, Velocity]	[Length]	3	7		
KNN	[Power, Velocity]	[Length]			2	
GB	[Power, Velocity]	[Length]	70	6		0.1
RF	[Power, Velocity]	[Width]	6	7		
ExtraTree	[Power, Velocity]	[Width]	8	8		
Bagging	[Power, Velocity]	[Width]	5	7		
KNN	[Power, Velocity]	[Width]			3	
GB	[Power, Velocity]	[Width]	80	4		0.1
RF	[Power, Velocity]	[Depth]	8	6		
ExtraTree	[Power, Velocity]	[Depth]	5	7		
Bagging	[Power, Velocity]	[Depth]	3	7		
KNN	[Power, Velocity]	[Depth]			4	
GB	[Power, Velocity]	[Depth]	80	5		0.1
RF	[Power, Velocity]	[Avg_Cross_Sectional_Area]	8	6		
ExtraTree	[Power, Velocity]	[Avg_Cross_Sectional_Area]	11	8		
Bagging	[Power, Velocity]	[Avg_Cross_Sectional_Area]	4	7		
KNN	[Power, Velocity]	[Avg_Cross_Sectional_Area]			3	
GB	[Power, Velocity]	[Avg_Cross_Sectional_Area]	4	9		
RF	[Power, Velocity]	[Avg_Meltpool_Volume]	8	9		
ExtraTree	[Power, Velocity]	[Avg_Meltpool_Volume]	11	8		
Bagging	[Power, Velocity]	[Avg_Meltpool_Volume]	4	9		
KNN	[Power, Velocity]	[Avg_Meltpool_Volume]			4	
GB	[Power, Velocity]	[Avg_Meltpool_Volume]	4	9		
RF	[Power, Velocity]	[Volume Indicated as Spatter]	6	5		
ExtraTree	[Power, Velocity]	[Volume Indicated as Spatter]	10	6		
Bagging	[Power, Velocity]	[Volume Indicated as Spatter]	6	4		
KNN	[Power, Velocity]	[Volume Indicated as Spatter]			5	
GB	[Power, Velocity]	[Volume Indicated as Spatter]	4	9		
RF	[Power, Velocity, log_Velocity]	[Volume Indicated as Spatter]	12	4		
ExtraTree	[Power, Velocity, log_Velocity]	[Volume Indicated as Spatter]	2	6		
Bagging	[Power, Velocity, log_Velocity]	[Volume Indicated as Spatter]	4	7		
KNN	[Power, Velocity, log_Velocity]	[Volume Indicated as Spatter]			5	
GB	[Power, Velocity, log_Velocity]	[Volume Indicated as Spatter]	21	4		
RF	[Length, Width, Depth]	[Volume Indicated as Spatter]	6	4		
ExtraTree	[Length, Width, Depth]	[Volume Indicated as Spatter]	30	6		
Bagging	[Length, Width, Depth]	[Volume Indicated as Spatter]	70	4		
KNN	[Length, Width, Depth]	[Volume Indicated as Spatter]			9	
GB	[Length, Width, Depth]	[Volume Indicated as Spatter]	35	2		0.1
RF	[log_Length, Width, Depth, log_Depth]	[Volume Indicated as Spatter]	6	4		
ExtraTree	[log_Length, Width, Depth, log_Depth]	[Volume Indicated as Spatter]	100	7		
Bagging	[log_Length, Width, Depth, log_Depth]	[Volume Indicated as Spatter]	7	5		
KNN	[log_Length, Width, Depth, log_Depth]	[Volume Indicated as Spatter]			8	
GB	[log_Length, Width, Depth, log_Depth]	[Volume Indicated as Spatter]	35	3		

Table 2: Performance evaluation of the ML models using the R^2 metric and mean absolute error (MAE) for both training and test datasets.

Model	Input	Output	R^2 (Train)	R^2 (Test)	Train MAE	Test MAE
RF	[Power, Velocity]	[Length]	0.9955	0.9611	6.1791	16.0696
ExtraTree	[Power, Velocity]	[Length]	0.9876	0.9557	10.4751	17.7457
Bagging	[Power, Velocity]	[Length]	0.9935	0.966	7.1818	15.0308
KNN	[Power, Velocity]	[Length]	0.9833	0.9681	14.1846	15.3929
GB	[Power, Velocity]	[Length]	0.9999	0.9598	1.0422	14.6793
RF	[Power, Velocity]	Width	0.983	0.9319	4.8998	9.9063
ExtraTree	[Power, Velocity]	Width	0.9899	0.9425	3.7299	8.6522
Bagging	[Power, Velocity]	Width	0.9824	0.9355	4.945	9.729
KNN	[Power, Velocity]	Width	0.9741	0.9109	6.2479	10.7778
GB	[Power, Velocity]	Width	0.9913	0.9374	3.6616	9.5184
RF	[Power, Velocity]	Depth	0.9948	0.9799	6.5786	12.8118
ExtraTree	[Power, Velocity]	Depth	0.9928	0.9889	7.0481	9.8546
Bagging	[Power, Velocity]	Depth	0.9932	0.9755	6.4861	14.3183
KNN	[Power, Velocity]	Depth	0.9935	0.9766	6.8679	12.1577
GB	[Power, Velocity]	Depth	0.9998	0.9868	1.4649	10.5286
RF	[Power, Velocity]	[Avg_Cross_Sectional_Area]	0.9968	0.988	662.3621	1438.8822
ExtraTree	[Power, Velocity]	[Avg_Cross_Sectional_Area]	0.9984	0.9913	534.358	1325.6511
Bagging	[Power, Velocity]	[Avg_Cross_Sectional_Area]	0.995	0.9844	891.3867	1712.9828
KNN	[Power, Velocity]	[Avg_Cross_Sectional_Area]	0.9948	0.9821	907.0427	1771.4683
GB	[Power, Velocity]	[Avg_Cross_Sectional_Area]	0.9954	0.9835	821.5204	1765.4271
RF	[Power, Velocity]	[Avg_Meltpool_Volume]	0.9983	0.9911	75125.5827	179674.6205
ExtraTree	[Power, Velocity]	[Avg_Meltpool_Volume]	0.999	0.9932	57304.9607	154726.1848
Bagging	[Power, Velocity]	[Avg_Meltpool_Volume]	0.9977	0.9903	80251.047	187474.9603
KNN	[Power, Velocity]	[Avg_Meltpool_Volume]	0.9909	0.9679	174572.6923	263140.1786
GB	[Power, Velocity]	[Avg_Meltpool_Volume]	0.9977	0.9903	80251.047	187474.9603
RF	['Power', 'Velocity']	['Volume Indicated as Spatter']	0.9414	0.8337	18709.6168	28853.8388
ExtraTree	[Power, Velocity]	['Volume Indicated as Spatter']	0.8918	0.796	22430.2771	31858.8664
Bagging	[Power, Velocity]	['Volume Indicated as Spatter']	0.9135	0.8206	23017.1701	30280.1787
KNN	[Power, Velocity]	['Volume Indicated as Spatter']	0.9057	0.8312	21643.8462	29152.9762
GB	[Power, Velocity]	['Volume Indicated as Spatter']	0.9352	0.8292	20081.6918	29010.1023
RF	[Power, Velocity, log_Velocity]	['Volume Indicated as Spatter']	0.9095	0.8006	23347.2729	30977.7348
ExtraTree	[Power, Velocity, log_Velocity]	['Volume Indicated as Spatter']	0.9435	0.8411	18106.0869	27507.3048
Bagging	[Power, Velocity, log_Velocity]	['Volume Indicated as Spatter']	0.9545	0.8399	14749.7506	27972.8045
KNN	[Power, Velocity, log_Velocity]	['Volume Indicated as Spatter']	0.9059	0.8159	21540.5128	30233.9286
GB	[Power, Velocity, log_Velocity]	['Volume Indicated as Spatter']	0.9252	0.8222	21730.3966	29863.3115
RF	[Length, Width, Depth]	['Volume Indicated as Spatter']	0.8698	0.7563	26654.2475	32366.5143
ExtraTree	[Length, Width, Depth]	['Volume Indicated as Spatter']	0.9045	0.801	23355.7838	30081.3716
Bagging	[Length, Width, Depth]	['Volume Indicated as Spatter']	0.8701	0.7624	26556.1096	31717.2
KNN	[Length, Width, Depth]	['Volume Indicated as Spatter']	0.8581	0.8233	27269.6581	27395.172
GB	[Length, Width, Depth]	['Volume Indicated as Spatter']	0.8559	0.7554	29410.0416	34711.6878
RF	[log_Length, Width, Depth, log_Depth]	['Volume Indicated as Spatter']	0.9033	0.8349	0.1924	0.2562
ExtraTree	[log_Length, Width, Depth, log_Depth]	['Volume Indicated as Spatter']	0.9677	0.8753	0.1112	0.2173
Bagging	[log_Length, Width, Depth, log_Depth]	['Volume Indicated as Spatter']	0.9263	0.831	0.174	0.2508
KNN	[log_Length, Width, Depth, log_Depth]	['Volume Indicated as Spatter']	0.7711	0.7508	0.3002	0.2856
GB	[log_Length, Width, Depth, log_Depth]	['Volume Indicated as Spatter']	0.9388	0.842	0.1597	0.2284

3.3. Polynomial regression prediction

To understand the relationship between the input and the output, polynomial regression was implemented, as it offers interpretability by breaking down the influence of each input variable and its interactions on the output prediction. This interpretability arises from the polynomial terms in the regression equation, where each term directly reflects the contribution of an input variable or a combination of variables to the overall prediction. Upon conducting polynomial fitting, where process conditions (power and velocity) were input while any of the melt pool dimension or geometry features served as the output, high performance was observed with training and testing R^2 exceeding 94%, as shown in Figures 4 and 5, respectively, and their values listed in Table 3 with the corresponding degree of polynomial implemented. The lowest performance among the melt pool dimension and geometry features was with respect to width (training R^2 : 95% and testing R^2 : 95%). Achieving the reported performance for width required using a higher-order polynomial (degree 5), indicating complexity in calculating the width as more interacting terms are involved.

A polynomial regression model was developed to predict the volume indicated as a spatter using four separate input features of which two sets of the process condition and the other two sets from melt pool dimensions: [Power, Velocity, and $\log(\text{Velocity})$] and [$\log(\text{length})$, width, depth, $\log(\text{width})$, and $\log(\text{depth})$], respectively. Logarithmic transformations were applied to the input process conditions and melt pool dimensions to enhance spatter prediction, as the logarithmic transformation can stabilize the variance across different ranges of the data. In addition, logarithmic transformations reduce skewness in variables. An improvement in both the training and the test accuracy was observed when a logarithmic transformation was applied to both the process condition and the input of the dimension of the melt pool. With respect to the process condition, we achieved increments of 8.4% and 5.3% in the training and testing R^2 values, respectively, by applying the logarithmic terms. A sixth-degree polynomial model was identified as the best fit, indicating the need to express complex

non-linear interactions between these features in the process conditions. Concurrently, an improvement in performance was observed when a logarithmic transformation was applied to the melt pool dimensions as input into the polynomial regression model. Training and testing R^2 increased by 6.3% and 15.5%, respectively, after the introduction of logarithmic terms.

The equations for different trained features are listed for the properties of the melt pool in Table 4, for the volume indicated as spatter in Tables 5 and Table A.6 in the Appendix. To quantify the importance of features in the equations, the absolute coefficients of the top contributing variables were extracted and their percentage contributions are shown in Figure 6. The generated equations indicate that the prediction of variables like length and depth depends more on the introduced power than on the velocity, while the width depends more on the velocity than on the power. At a particular velocity, the depth or length value will intuitively depend on the applied power, since the power influences the dynamics of the melt pool, the amount of liquid fraction and the rate of solidification. However, the fact that velocity has a stronger importance than power for the width suggests a low sensitivity of power over a wide range of velocities, as the melt pool motion and temperature gradient are influenced, making the stabilization of the width more dependent on velocity. The greater magnitude of length and depth range compared to width range, as shown in Figure 2 in the investigated process conditions, could have led to the strong importance of power in the geometry features of the melt pool (cross-sectional area and volume). Since the influence of power is more dominant in the equations for both length and depth, the dependency of the volume of the melt pool on these variables is likely influenced by power, as observed in Figure 6E. The effect of width, being more influenced by velocity, arises from the cross-sectional area but is not strong enough to dominate over the power. The term Velocity² is the most important variable for the predicted volume indicated as spatter when the process condition was used as the input of the model, as shown in Figure 6F. Upon applying a

logarithmic transformation to the process condition in Figure 6G, it was found that the top two ranking variables are "Power³, Velocity" and "Power³, log(Velocity)", indicating that they are highly influential in determining the volume indicated as a spatter when a logarithmic transformation is applied to the process conditions. In the case of applying the dimensions of the melt pool as input to the regression model, it was found that the width followed by the depth is the most important, as shown in Figure 6H. Upon applying a logarithmic transformation to the dimension of the melt pool in Figure 6 I, the width derivative in the form of $\log(\text{width})$ and $\log(\text{width})^2$ was found to be the first two variables to be most significant, indicating the prominent role of width before and after applying the logarithmic transformation to the prediction of volume indicated as spatter.

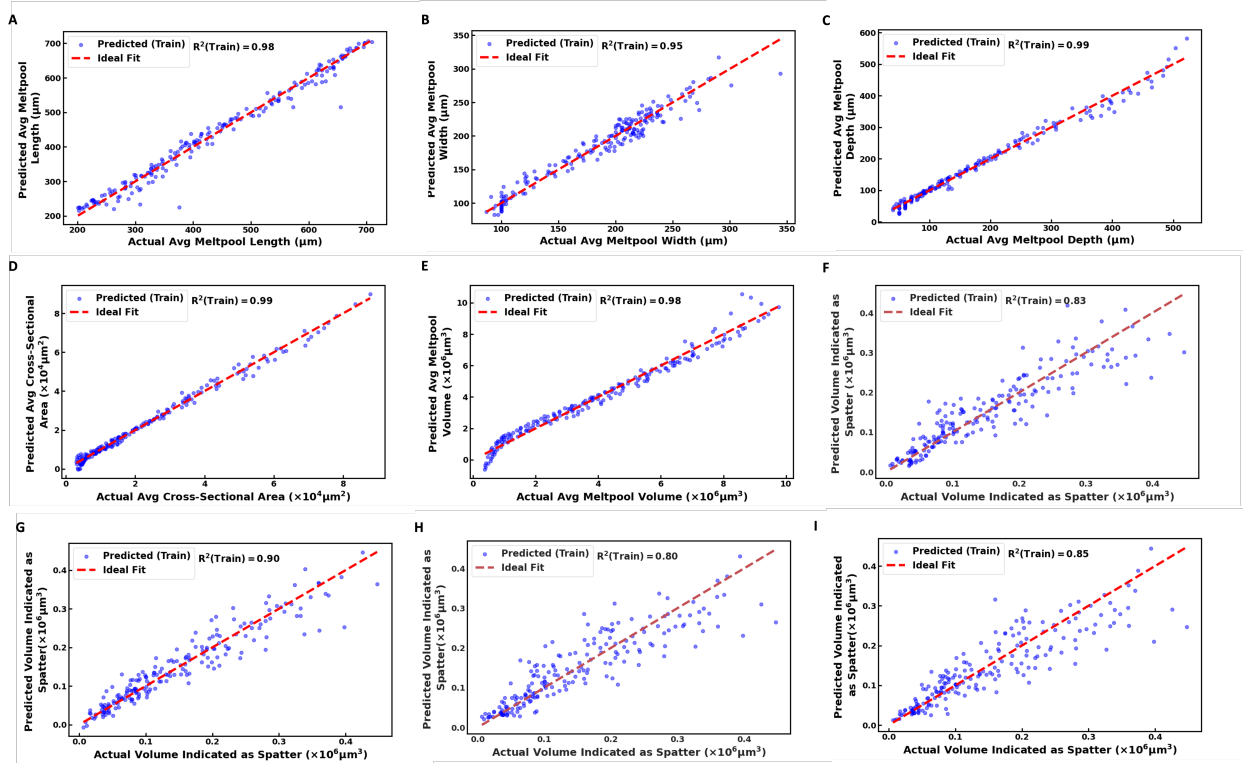


Figure 4: Polynomial regression fitting on the training dataset using either process conditions or melt pool dimension as an input into the model to predict the following (A) Melt pool length prediction using power and velocity as the model input (B) Melt pool width prediction using power and velocity as the model input (C) Melt pool depth prediction using power and velocity as the model input (D) Melt pool top cross sectional area prediction using power and velocity as the model input (E) Melt pool volume prediction using power and velocity as the model input (F) Prediction of volume indicated as spatter using power and velocity as the model input (G) Prediction of volume indicated as spatter using power and velocity as the model input (H) Prediction of volume indicated as spatter using Power, Velocity, and $\log(\text{Velocity})$ as the model input (I) Prediction of volume indicated as spatter using length, width and depth as the model input (J) Prediction of volume indicated as spatter using $\log(\text{length})$, width, depth, $\log(\text{width})$, and $\log(\text{depth})$ as the model input

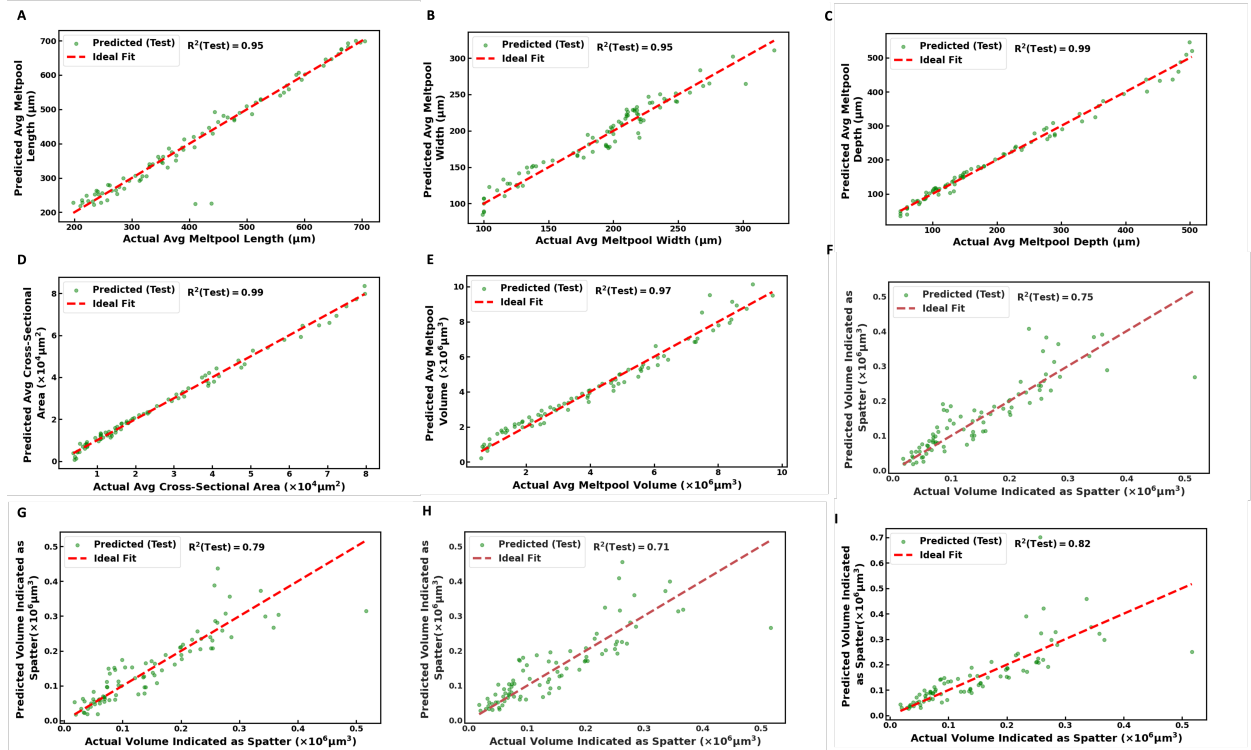


Figure 5: Polynomial regression fitting for the test dataset (A) Melt pool length prediction using power and velocity as the model input (B) Melt pool width prediction using power and velocity as the model input (C) Melt pool depth prediction using power and velocity as the model input (D) Melt pool top cross sectional area prediction using power and velocity as the model input (E) Melt pool volume prediction using power and velocity as the model input (F) Prediction of volume indicated as spatter using power and velocity as the model input (G) Prediction of volume indicated as spatter using power and velocity as the model input (H) Prediction of volume indicated as spatter using Power, Velocity, and $\log(\text{Velocity})$ as the model input (I) Prediction of volume indicated as spatter using length, width and depth as the model input (J) Prediction of volume indicated as spatter using log(length), width, depth, $\log(\text{width})$, and $\log(\text{depth})$ as the model input

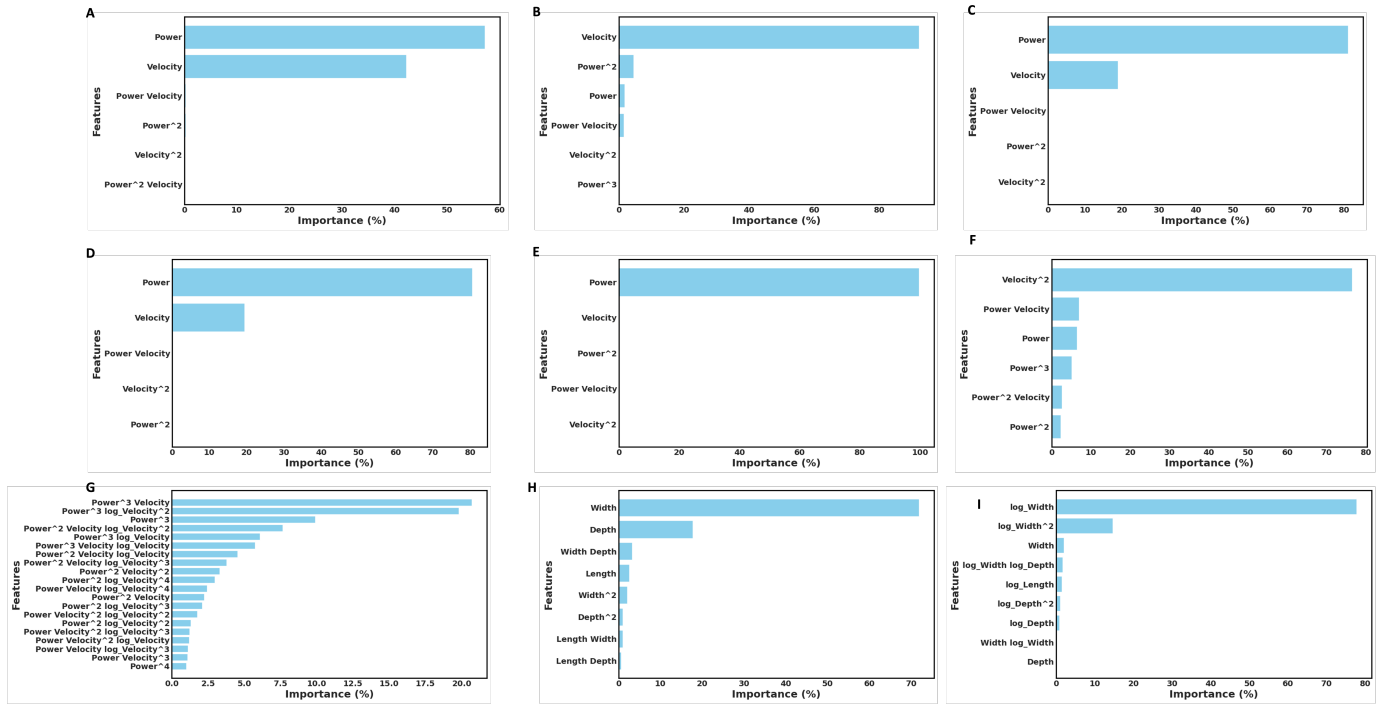


Figure 6: Display of the top feature importances from the derived equation in polynomial regression (A) Melt pool length prediction using power and velocity as the model input (B) Melt pool width prediction using power and velocity as the model input (C) Melt pool depth prediction using power and velocity as the model input (D) Melt pool top cross sectional area prediction using power and velocity as the model input (E) Melt pool volume prediction using power and velocity as the model input (F) Prediction of volume indicated as spatter using power and velocity as the model input (G) Prediction of volume indicated as spatter using Power, Velocity, and $\log(\text{Velocity})$ as the model input (H) Prediction of volume indicated as spatter using length, width and depth as the model input (I) Prediction of volume indicated as spatter using $\log(\text{length})$, width, depth, $\log(\text{width})$, and $\log(\text{depth})$ as the model input

Table 3: Performance of polynomial regression model with the degree of the polynomial in predicting melt pool dimensions, geometry and volume indicated as spatter

Input	Predicted Features	Order	R ² (Train)	R ² (Test)
[Power, Velocity]	Avg Meltpool Length	3	0.98	0.95
[Power, Velocity]	Avg Meltpool Width	5	0.95	0.95
[Power, Velocity]	Avg Meltpool Depth	2	0.99	0.99
[Power, Velocity]	Avg Cross Sectional Area	2	0.99	0.99
[Power, Velocity]	Avg Meltpool Volume	2	0.98	0.97
[Power, Velocity]	Volume Indicated as Spatter	6	0.83	0.75
[Power, Velocity, log Velocity]	Volume Indicated as Spatter	6	0.9	0.79
[Length, Width, Depth]	Volume Indicated as Spatter	3	0.8	0.71
[log Length, Width, Depth, log Width, log Depth]	Volume Indicated as Spatter	2	0.85	0.82

Table 4: Polynomial regression equations for melt pool dimensions and geometry features

Features	Equation	R ² (Train)
Length	$170.3876 + 0.7513P - 0.5552V - 0.0032P^2 + 0.0034PV + 5.40 \times 10^{-4}V^2 + 4.19 \times 10^{-6}P^3 - 4.83 \times 10^{-6}P^2V + 4.49 \times 10^{-7}PV^2 - 3.46 \times 10^{-7}V^3$	0.98
Width	$14.7778 - 0.0065P + 0.3516V + 0.0173P^2 - 0.0056PV + 1.94 \times 10^{-4}V^2 - 9.14 \times 10^{-5}P^3 + 3.31 \times 10^{-5}P^2V - 4.99 \times 10^{-6}PV^2 - 1.35 \times 10^{-7}V^3 + 1.96 \times 10^{-7}P^4 - 1.12 \times 10^{-7}P^3V + 3.67 \times 10^{-8}P^2V^2 - 4.82 \times 10^{-9}PV^3 + 7.74 \times 10^{-10}V^4$	0.95
Depth	$53.7694 + 1.5055P - 0.3504V - 2.92 \times 10^{-4}P^2 - 7.54 \times 10^{-4}PV + 2.12 \times 10^{-4}V^2$	0.99
Area	$4176.5581 + 224.9810P - 54.3024V - 0.0011P^2 - 0.1333PV + 0.0353V^2$	0.99
Volume	$-1262141.6793 + 21113.6671P + 7.5091V + 17.3061P^2 - 9.5400PV - 0.4026V^2$	0.98

Table 5: Polynomial regression equations for melt pool volume indicated as spatter, as the equations are derived from the model input

Features	Equation	R^2 (Train)
Spatter	$-47591.2675 - 0.1273 - 0.2616P - 0.0237V - 0.0944P^2 + 0.2825PV + 3.0756V^2 + 0.2039P^3 - 0.1063P^2V + 0.0093PV^2 - 0.0102V^3 - 0.0014P^4 + 5.58 \times 10^{-4}P^3V + 3.93 \times 10^{-5}P^2V^2 - 1.76 \times 10^{-5}PV^3 + 1.47 \times 10^{-5}V^4 + 3.68 \times 10^{-6}P^5 - 1.14 \times 10^{-6}P^4V - 2.27 \times 10^{-7}P^3V^2 + 6.23 \times 10^{-8}P^2V^3 - 2.26 \times 10^{-9}PV^4 - 8.52 \times 10^{-9}V^5 - 3.32 \times 10^{-9}P^6 + 1.26 \times 10^{-9}P^5V - 2.78 \times 10^{-10}P^4V^2 + 2.47 \times 10^{-10}P^3V^3 - 8.39 \times 10^{-11}P^2V^4 + 1.11 \times 10^{-11}PV^5 + 1.42 \times 10^{-12}V^6$	0.83
Spatter	$-73673.5843 + 60.4532L + 1719.4559W + 424.9562D + 1.6502L^2 - 23.3099LW + 14.7747LD + 48.4069W^2 - 77.2674WD + 24.4086D^2 - 0.0070L^3 + 0.0752L^2W - 0.0317L^2D - 0.1816LW^2 + 0.1530LWD - 0.0400LD^2 + 0.0515W^3 + 0.0234W^2D - 0.0140WD^2 - 0.0023D^3$	0.8
Spatter	$-1262141.6793 - 34.2697 \log L + 46.6761W + 3.3128D + 1832.5419 \log W - 19.5423 \log D + 2.0622(\log L)^2 - 0.0189 \log L \cdot W + 6.79 \times 10^{-4} \log L \cdot D + 1.5434 \log L \cdot \log W + 1.1827 \log L \cdot \log D + 0.0032W^2 + 0.0011WD - 6.1771W \cdot \log W - 0.1413W \cdot \log D + 1.73 \times 10^{-5}D^2 - 0.3015D \cdot \log W - 0.2274D \cdot \log D - 347.0129(\log W)^2 + 40.4521 \log W \cdot \log D - 26.0121(\log D)^2$	0.85

4. Conclusions

In this work, we analyze a spatter dataset collected by coupling OpenFOAM and FLOW-3D, leveraging the strengths of both simulation packages. OpenFOAM generates realistic spatter occurrences but is computationally expensive, while FLOW-3D is computationally efficient but lacks the physics to produce realistic spatter phenomena. With this configuration, we collected a dataset comprising melt pool length, width, depth, cross-sectional area, volume, and volume indicated as spatter. The performance of machine learning models and polynomial regression was evaluated on the collected parameters, showing high accuracy of 95% and above for melt pool dimensions and geometry features for both ML models and polynomial fitting. For predicting the volume indicated as spatter, the Extra-Trees model achieved the highest R^2 scores of 0.97 and 0.88 for the training and testing datasets, respectively. Using polynomial fitting, we derived equations for each melt pool dimension,

geometry, and volume indicated as spatter based on model inputs, enhancing interpretability by showing how input variables influence the outputs. This findings open opportunities for robust control systems to monitor part production, minimize defect formation, and ensure repeatability in AM processes.

Declarations

Funding

This research was sponsored by the Army Research Laboratory and conducted under Cooperative Agreement Number W911NF-20-2-0175. The views and conclusions presented in this document are those of the authors and do not necessarily represent the official policies or positions of the Army Research Laboratory or the U.S. Government. The U.S. Government is authorized to reproduce and distribute reprints for governmental purposes, despite any copyright notice herein.

Competing Interests

The authors have no competing interests to declare that are relevant to the content of this article.

References

- [1] Jingchang Li, Qi Zhou, Longchao Cao, Yanzhi Wang, and Jiexiang Hu. A convolutional neural network-based multi-sensor fusion approach for in-situ quality monitoring of selective laser melting. *Journal of Manufacturing Systems*, 64:429–442, 2022.
- [2] Florian Wirth, Teresa Tonn, Markus Schöberl, Stefan Hermann, Hannes Birkhofer, and Vasily Ploshikhin. Implementation of the marangoni effect in an open-source software environment and the influence of surface tension modeling in the mushy region in laser powder bed fusion (lpbf). *Modelling and Simulation in Materials Science and Engineering*, 30(3):034001, 2022.
- [3] Giulia Repossini, Vittorio Laguzza, Marco Grasso, and Bianca Maria Colosimo. On the use of spatter signature for in-situ monitoring of laser powder bed fusion. *Additive Manufacturing*, 16:35–48, 2017.

[4] Yaohong Xiao, Xiantong Wang, Wenhua Yang, XinXin Yao, Zhuo Yang, Yan Lu, Zuo Wang, and Lei Chen. Data-driven prediction of future melt pool from built parts during metal additive manufacturing. *Additive Manufacturing*, page 104438, 2024.

[5] Olabode T Ajenifujah, Francis Ogoke, Florian Wirth, Jack Beuth, and Amir Barati Farimani. Integrating multi-physics simulations and machine learning to define the spatter mechanism and process window in laser powder bed fusion. *arXiv preprint arXiv:2405.07823*, 2024.

[6] GL Knapp, Tuhin Mukherjee, JS Zuback, HL Wei, TA Palmer, Amitava De, and TJAM DebRoy. Building blocks for a digital twin of additive manufacturing. *Acta Materialia*, 135:390–399, 2017.

[7] Li Zhang, Xiaoqi Chen, Wei Zhou, Taobo Cheng, Lijia Chen, Zhen Guo, Bing Han, and Longxing Lu. Digital twins for additive manufacturing: a state-of-the-art review. *Applied Sciences*, 10(23):8350, 2020.

[8] Zhiqiang Wang, Xuede Wang, Xin Zhou, Guangzhao Ye, Xing Cheng, and Peiyu Zhang. Investigation into spatter particles and their effect on the formation quality during selective laser melting processes. *CMES-Computer Modeling in Engineering & Sciences*, 124(1), 2020.

[9] Francis Ogoke, Quanliang Liu, Olabode Ajenifujah, Alexander Myers, Guadalupe Quirarte, Jonathan Malen, Jack Beuth, and Amir Barati Farimani. Inexpensive high fidelity melt pool models in additive manufacturing using generative deep diffusion. *Materials & Design*, 245:113181, 2024.

[10] Ross Cunningham, Sneha P Narra, Colt Montgomery, Jack Beuth, and AD Rollett. Synchrotron-based x-ray microtomography characterization of the effect of processing variables on porosity formation in laser power-bed additive manufacturing of ti-6al-4v. *Jom*, 69:479–484, 2017.

[11] Yunhui Chen, Samuel Clark, ACL Leung, L Sinclair, S Marussi, Robert Atwood, T Connolley, Martyn Jones, G Baxter, and PD Lee. Melt pool morphology in directed energy deposition additive manufacturing process. In *IOP conference series: materials science and engineering*, volume 861, page 012012. IOP Publishing, 2020.

[12] Andrew M Kiss, Anthony Y Fong, Nicholas P Calta, Vivek Thampy, Aiden A Martin, Philip J Depond, Jenny Wang, Manyalibo J Matthews, Ryan T Ott, Christopher J Tassone, et al. Laser-induced keyhole defect dynamics during metal additive manufacturing. *Advanced Engineering Materials*, 21(10):1900455, 2019.

[13] Qilin Guo, Cang Zhao, Minglei Qu, Lianghua Xiong, Luis I Escano, S Mohammad H Hojjatzadeh, Niranjan D Parab, Kamel Fezzaa, Wes Everhart, Tao Sun, et al. In-situ characterization and quantification of melt pool variation under constant input energy density in laser powder bed fusion additive

manufacturing process. *Additive Manufacturing*, 28:600–609, 2019.

- [14] Jian Tang, Rafal Wróbel, Pooriya Scheel, Willy Gaechter, Christian Leinenbach, and Ehsan Hosseini. The role of process parameters and printing position on melt pool variations in lpbf hastelloy x: Insights into laser-plume interaction. *Additive Manufacturing Letters*, 9:100203, 2024.
- [15] RK Leach, David Bourell, Simone Carmignato, Alkan Donmez, Nicola Senin, and Wim Dewulf. Geometrical metrology for metal additive manufacturing. *CIRP annals*, 68(2):677–700, 2019.
- [16] Joni Reijonen, Alejandro Revuelta, Sini Metsä-Kortelainen, and Antti Salminen. Effect of laser focal point position on porosity and melt pool geometry in laser powder bed fusion additive manufacturing. *Additive Manufacturing*, 85:104180, 2024.
- [17] Shuheng Liao, Tianju Xue, and Jian Cao. Deep learning based reconstruction of transient 3d melt pool geometries in laser powder bed fusion from coaxial melt pool images. *Manufacturing Letters*, 40:50–53, 2024.
- [18] Amir Barati Farimani, Peter Pak, et al. Llm-3d print: Large language models to monitor and control 3d printing. 2024.
- [19] Luke Scime and Jack Beuth. Melt pool geometry and morphology variability for the inconel 718 alloy in a laser powder bed fusion additive manufacturing process. *Additive Manufacturing*, 29:100830, 2019.
- [20] Zhaorui Yan, Weiwei Liu, Zijue Tang, Xuyang Liu, Nan Zhang, Mingzheng Li, and Hongchao Zhang. Review on thermal analysis in laser-based additive manufacturing. *Optics & Laser Technology*, 106:427–441, 2018.
- [21] Alexander J Myers, Guadalupe Quirarte, Francis Ogoke, Brandon M Lane, Syed Zia Uddin, Amir Barati Farimani, Jack L Beuth, and Jonathan A Malen. High-resolution melt pool thermal imaging for metals additive manufacturing using the two-color method with a color camera. *Additive Manufacturing*, 73:103663, 2023.
- [22] Alexander J Myers, Guadalupe Quirarte, Jack L Beuth, and Jonathan A Malen. Two-color thermal imaging of the melt pool in powder-blown laser-directed energy deposition. *Additive Manufacturing*, 78:103855, 2023.
- [23] Shyam Barua, Frank Liou, Joseph Newkirk, and Todd Sparks. Vision-based defect detection in laser metal deposition process. *Rapid Prototyping Journal*, 20(1):77–85, 2014.
- [24] Tatsuhiko Kuriya, Ryo Koike, Takanori Mori, and Yasuhiro Kakinuma. Relationship between solidification time and porosity with directed energy deposition of inconel 718. *Journal of Advanced Mechanical Design, Systems, and Manufacturing*, 12(5):JAMDSM0104–JAMDSM0104, 2018.

[25] AmirPouya Hemmasian, Francis Ogoke, Parand Akbari, Jonathan Malen, Jack Beuth, and Amir Barati Farimani. Surrogate modeling of melt pool temperature field using deep learning. *Additive Manufacturing Letters*, 5:100123, 2023.

[26] Mojtaba Khanzadeh, Wenmeng Tian, Aref Yadollahi, Haley R Doude, Mark A Tschopp, and Linkan Bian. Dual process monitoring of metal-based additive manufacturing using tensor decomposition of thermal image streams. *Additive Manufacturing*, 23:443–456, 2018.

[27] Hou Yi Chia, Yanming Zhang, Lu Wang, and Wentao Yan. Unveiling gas–liquid metal reactions in metal additive manufacturing: High-fidelity modeling validated with experiments. *Acta Materialia*, 275:120029, 2024.

[28] Du-Rim Eo, Seong Gyu Chung, Jin Myoung Jeon, and Jung-Wook Cho. Melt pool oxidation and reduction in powder bed fusion. *Additive Manufacturing*, 41:101982, 2021.

[29] Nicholas P Calta, Aiden A Martin, Joshua A Hammons, Michael H Nielsen, Tien T Roehling, Kamel Fezzaa, Manyalibo J Matthews, Jason R Jeffries, Trevor M Willey, and Jonathan RI Lee. Pressure dependence of the laser–metal interaction under laser powder bed fusion conditions probed by in situ x-ray imaging. *Additive Manufacturing*, 32:101084, 2020.

[30] Chu Lun Alex Leung, Sebastian Marussi, Michael Towrie, Robert C Atwood, Philip J Withers, and Peter D Lee. The effect of powder oxidation on defect formation in laser additive manufacturing. *Acta Materialia*, 166:294–305, 2019.

[31] Gowtham Soundarapandian, Chu Lun Alex Leung, Carol Johnston, Bo Chen, Raja HU Khan, Phil McNutt, Alisha Bhatt, Robert C Atwood, Peter D Lee, and Michael E Fitzpatrick. In situ monitoring the effects of ti6al4v powder oxidation during laser powder bed fusion additive manufacturing. *International Journal of Machine Tools and Manufacture*, 190:104049, 2023.

[32] Parand Akbari, Francis Ogoke, Ning-Yu Kao, Kazem Meidani, Chun-Yu Yeh, William Lee, and Amir Barati Farimani. Meltpoolnet: Melt pool characteristic prediction in metal additive manufacturing using machine learning. *Additive Manufacturing*, 55:102817, 2022.

[33] Zhibo Zhang, Chandan Kumar Sahu, Shubhendu Kumar Singh, Rahul Rai, Zhuo Yang, and Yan Lu. Machine learning based prediction of melt pool morphology in a laser-based powder bed fusion additive manufacturing process. *International Journal of Production Research*, 62(5):1803–1817, 2024.

[34] Rongxuan Wang, Ruixuan Wang, Chaoran Dou, Shuo Yang, Raghav Gnanasambandam, Anbo Wang, and Zhenyu Kong. Sub-surface thermal measurement in additive manufacturing via machine learning-enabled high-resolution fiber optic sensing. *Nature Communications*, 15(1):7568, 2024.

[35] Luke Scime and Jack Beuth. Using machine learning to identify in-situ melt pool signatures indicative of flaw formation in a laser powder bed fusion additive manufacturing process. *Additive Manufacturing*, 25:151–165, 2019.

[36] Mohsen Taheri Andani, Reza Dehghani, Mohammad Reza Karamooz-Ravari, Reza Mirzaefar, and Jun Ni. Spatter formation in selective laser melting process using multi-laser technology. *Materials & Design*, 131:460–469, 2017.

[37] Mohsen Taheri Andani, Reza Dehghani, Mohammad Reza Karamooz-Ravari, Reza Mirzaefar, and Jun Ni. A study on the effect of energy input on spatter particles creation during selective laser melting process. *Additive Manufacturing*, 20:33–43, 2018.

[38] Luis E Criales, Yiğit M Arisoy, Brandon Lane, Shawn Moylan, Alkan Donmez, and Tuğrul Özel. Laser powder bed fusion of nickel alloy 625: Experimental investigations of effects of process parameters on melt pool size and shape with spatter analysis. *International Journal of Machine Tools and Manufacture*, 121:22–36, 2017.

[39] Reza Esmaeilizadeh, Usman Ali, Ali Keshavarzkermani, Yahya Mahmoodkhani, Ehsan Marzbanrad, and Ehsan Toyserkani. On the effect of spatter particles distribution on the quality of hastelloy x parts made by laser powder-bed fusion additive manufacturing. *Journal of Manufacturing Processes*, 37:11–20, 2019.

[40] JL Otegui, HW Kerr, DJ Burns, and UH Mohaupt. Fatigue crack initiation from defects at weld toes in steel. *International journal of pressure vessels and piping*, 38(5):385–417, 1989.

[41] Dongsen Ye, Kunpeng Zhu, Jerry Ying Hsi Fuh, Yingjie Zhang, and Hong Geok Soon. The investigation of plume and spatter signatures on melted states in selective laser melting. *Optics & Laser Technology*, 111:395–406, 2019.

[42] Gwenaelle Chebil, Dimitri Bettebghor, Yves Renollet, P Lapouge, Cecile Davoine, Marc Thomas, V Favier, and M Schneider. Deep learning object detection for optical monitoring of spatters in l-pbf. *Journal of Materials Processing Technology*, 319:118063, 2023.

[43] Wang Cai, LeShi Shu, ShaoNing Geng, Qi Zhou, and LongChao Cao. Real-time tracking method for motion spatter in high-power laser welding of stainless steel plate based on a lightweight deep learning model. *Expert Systems with Applications*, page 124386, 2024.

[44] Ziqian Wu, Zhenying Xu, and Wei Fan. Online detection of powder spatters in the additive manufacturing process. *Measurement*, 194:111040, 2022.

[45] Di Wang, Wenhao Dou, Yuanhui Ou, Yongqiang Yang, Chaolin Tan, and Yingjie Zhang. Characteristics

of droplet spatter behavior and process-correlated mapping model in laser powder bed fusion. *Journal of materials research and technology*, 12:1051–1064, 2021.

[46] Nicholas O’Brien, Syed Zia Uddin, Jordan Weaver, Jake Jones, Satbir Singh, and Jack Beuth. Computational analysis and experiments of spatter transport in a laser powder bed fusion machine. *Additive Manufacturing*, page 104133, 2024.

[47] Minglei Qu, Qilin Guo, Luis I Escano, Ali Nabaa, S Mohammad H Hojjatzadeh, Zachary A Young, and Lianyi Chen. Controlling process instability for defect lean metal additive manufacturing. *Nature communications*, 13(1):1079, 2022.

[48] Bo Cheng, Lukas Loeber, Hannes Willeck, Udo Hartel, and Charles Tuffile. Computational investigation of melt pool process dynamics and pore formation in laser powder bed fusion. *Journal of Materials Engineering and Performance*, 28:6565–6578, 2019.

[49] Jennifer Lundkvist. Cfd simulation of fluid flow during laser metal wire deposition using openfoam: 3d printing, 2019.

[50] OpenCFD Ltd (ESI Group). Openfoam documentation. (online) <https://www.openfoam.com/documentation/overview>.

[51] Francis Ogoke, William Lee, Ning-Yu Kao, Alexander Myers, Jack Beuth, Jonathan Malen, and Amir Barati Farimani. Convolutional neural networks for melt depth prediction and visualization in laser powder bed fusion. *The International Journal of Advanced Manufacturing Technology*, 129(7):3047–3062, 2023.

[52] Peter S Cook and Anthony B Murphy. Simulation of melt pool behaviour during additive manufacturing: Underlying physics and progress. *Additive Manufacturing*, 31:100909, 2020.

[53] Leo Breiman. Random forests. *Machine learning*, 45(1):5–32, 2001.

[54] Trevor Hastie. The elements of statistical learning: data mining, inference, and prediction, 2009.

[55] A Liaw. Classification and regression by randomforest. *R news*, 2002.

[56] Pierre Geurts, Damien Ernst, and Louis Wehenkel. Extremely randomized trees. *Machine learning*, 63(1):3–42, 2006.

[57] Fabian Pedregosa. Scikit-learn: Machine learning in python fabian. *Journal of machine learning research*, 12:2825, 2011.

[58] Leo Breiman. Bagging predictors. *Machine learning*, 24(2):123–140, 1996.

[59] Naomi S Altman. An introduction to kernel and nearest-neighbor nonparametric regression. *The American Statistician*, 46(3):175–185, 1992.

- [60] Thomas Cover and Peter Hart. Nearest neighbor pattern classification. *IEEE transactions on information theory*, 13(1):21–27, 1967.
- [61] Jerome H Friedman. Greedy function approximation: a gradient boosting machine. *Annals of statistics*, pages 1189–1232, 2001.
- [62] Alexey Natekin and Alois Knoll. Gradient boosting machines, a tutorial. *Frontiers in neurorobotics*, 7:21, 2013.

Appendix A. OpenFOAM simulation domain

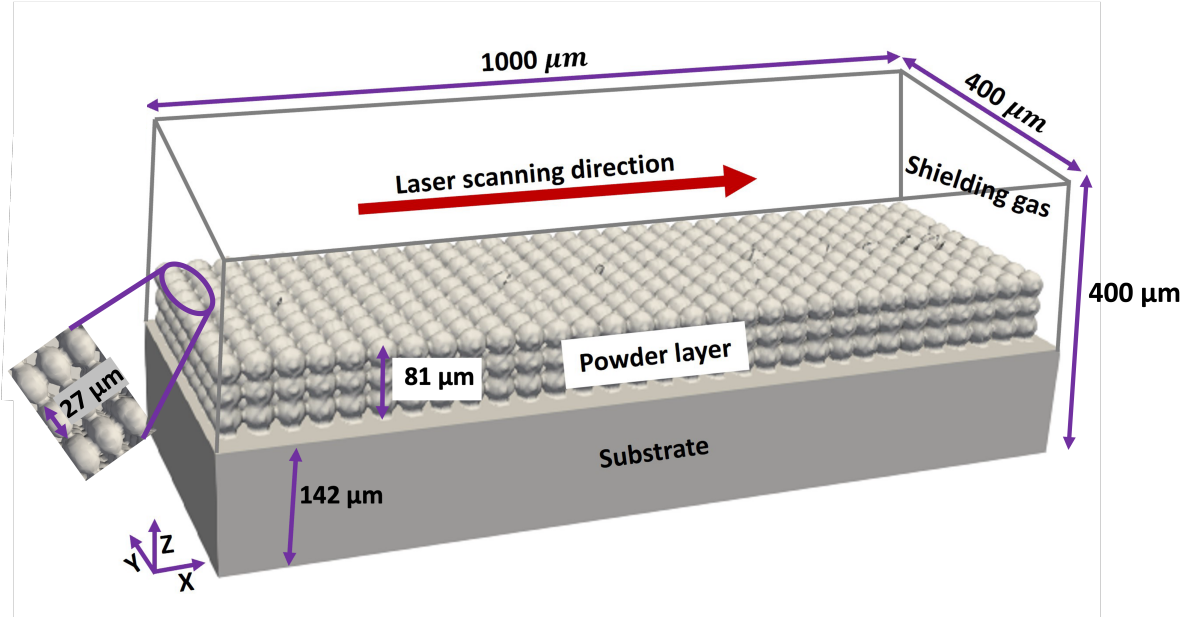


Figure A.7: Schematic illustration of the computational domain with random packing of Stainless steel powder bed.

Appendix A.1. Machine learning prediction

Appendix A.1.1. Random Forest (RF)

Random forest regression is an ensemble method that enhances predictive accuracy by averaging multiple decision trees, which reduces overfitting [53]. This technique leverages random sampling of data and features, capturing complex interactions and improving generalization [54]. Known for its robustness in high-dimensional, nonlinear datasets, random forests also provide insights into feature importance, aiding model interpretability[55].

Appendix A.1.2. The Extra Trees Regressor

The Extra Trees Regressor, or Extremely Randomized Trees, is an ensemble method similar to random forests but introduces more randomness to improve performance and reduce variance [56]. Instead of selecting optimal split points, it randomly chooses split

thresholds for each feature, which leads to greater diversity among trees and often faster training. This approach enhances generalization and can handle complex, high-dimensional data efficiently, though it may require careful tuning to avoid underfitting in some cases [57].

Appendix A.1.3. Bagging Regressor

The Bagging Regressor is an ensemble method that improves prediction accuracy by combining the outputs of multiple base regressors trained on randomly sampled subsets of the data [58]. This technique, also known as bootstrap aggregation, reduces model variance and enhances generalization by averaging the predictions of each model, often resulting in more robust performance compared to a single model [54]. Bagging is particularly effective for high-variance models, such as decision trees, and can be customized with different base regressors to suit various tasks.

Appendix A.1.4. The K-Nearest Neighbors (KNN) Regressor

KNN Regressor is a non-parametric method that predicts the value of a target variable based on the average of its k closest data points (neighbors) in the feature space [59]. This approach is simple and effective for datasets where similar instances yield similar outputs, but its performance can be affected by high-dimensional data and may require scaling to handle features of different units effectively. The choice of k impacts the model's bias-variance trade-off, with smaller values leading to more variance and larger values resulting in smoother, potentially biased predictions [60].

Appendix A.1.5. The Gradient Boosting (GB) Regressor

The Gradient Boosting Regressor is an ensemble learning method that builds a sequence of weak learners, typically decision trees, where each subsequent model corrects the errors of its predecessor [61]. By minimizing a loss function through gradient descent, it achieves high accuracy and handles complex, non-linear relationships well. Known for its robustness

and predictive power, gradient boosting is effective in both small and large datasets, though it requires careful tuning to prevent overfitting and can be computationally intensive [62].

Table A.6: Polynomial regression equations for melt pool volume indicated as spatter, as the equation is derived from logarithm transformation of melt pool dimension

Features	Equation	R ² (Train)
Spatter	$\begin{aligned} & -94877.9016 + 0.0016P - 0.0113V - 0.0131 \log V + 0.0192P^2 - \\ & 0.0054PV + 0.0023P \log V - 0.0043V^2 - 2.81 \times 10^{-4}V \log V - \\ & 6.35 \times 10^{-4}(\log V)^2 + 0.3343P^3 + 0.0824P^2V + 0.0351P^2 \log V - \\ & 0.0297PV^2 - 0.0093PV \log V + 1.98 \times 10^{-4}P(\log V)^2 - 0.0378V^3 - \\ & 0.0140V^2 \log V - 0.0019V(\log V)^2 - 1.05 \times 10^{-4}(\log V)^3 - 0.0303P^4 + \\ & 0.7149P^3V + 0.2123P^3 \log V + 0.0801P^2V^2 + 0.0937P^2V \log V + \\ & 0.0668P^2(\log V)^2 - 0.1631PV^3 - 0.0153PV^2 \log V - \\ & 0.0357PV(\log V)^2 - 0.0020P(\log V)^3 + 0.0014V^4 - \\ & 0.0473V^3 \log V - 0.0347V^2(\log V)^2 - 0.0075V(\log V)^3 - 5.44 \times \\ & 10^{-4}(\log V)^4 + 6.57 \times 10^{-6}P^5 + 2.25 \times 10^{-4}P^4V + 0.0143P^4 \log V - \\ & 7.38 \times 10^{-4}P^3V^2 - 0.2463P^3V \log V - 0.6532P^3(\log V)^2 + 1.34 \times \\ & 10^{-4}P^2V^3 - 0.0214P^2V^2 \log V + 0.0456P^2V(\log V)^2 + \\ & 0.0618P^2(\log V)^3 - 1.87 \times 10^{-5}PV^4 + 0.0427PV^3 \log V + \\ & 0.1350PV^2(\log V)^2 - 0.0936PV(\log V)^3 - 0.0160P(\log V)^4 - 1.04 \times \\ & 10^{-6}V^5 - 0.0018V^4 \log V - 0.0172V^3(\log V)^2 - 0.0543V^2(\log V)^3 - \\ & 0.0257V(\log V)^4 - 0.0026(\log V)^5 + 2.08 \times 10^{-9}P^6 + 6.55 \times \\ & 10^{-9}P^5V - 2.34 \times 10^{-6}P^5 \log V + 8.67 \times 10^{-9}P^4V^2 - 2.98 \times \\ & 10^{-5}P^4V \log V - 0.0020P^4(\log V)^2 - 1.53 \times 10^{-8}P^3V^3 + 8.50 \times \\ & 10^{-5}P^3V^2 \log V + 0.0244P^3V(\log V)^2 + 0.0579P^3(\log V)^3 + 5.18 \times \\ & 10^{-9}P^2V^4 - 1.74 \times 10^{-5}P^2V^3 \log V + 0.0010P^2V^2(\log V)^2 - \\ & 0.0073P^2V(\log V)^3 - 0.1802P^2(\log V)^4 - 1.17 \times 10^{-9}PV^5 + 2.95 \times \\ & 10^{-6}PV^4 \log V - 0.0029PV^3(\log V)^2 + 0.0018PV^2(\log V)^3 - \\ & 0.0679PV(\log V)^4 - 0.0785P(\log V)^5 + 9.03 \times 10^{-11}V^6 + 1.59 \times \\ & 10^{-8}V^5 \log V + 2.22 \times 10^{-4}V^4(\log V)^2 + 0.0071V^3(\log V)^3 + \\ & 0.0482V^2(\log V)^4 - 0.0750V(\log V)^5 - 0.0110(\log V)^6 \end{aligned}$	0.9